

Selective Attenuation of Lightning-Generated Whistlers at Extralow Frequencies: DEMETER Spacecraft Observations

J. Záhlava, F. Němec, O. Santolík, I. Kolmašová, Michel Parrot, D. Kouba

▶ **To cite this version:**

J. Záhlava, F. Němec, O. Santolík, I. Kolmašová, Michel Parrot, et al.. Selective Attenuation of Lightning-Generated Whistlers at Extralow Frequencies: DEMETER Spacecraft Observations. Journal of Geophysical Research Space Physics, 2018, 123 (10), pp.8631-8640. 10.1029/2018JA025879 . insu-03217099

HAL Id: insu-03217099

https://insu.hal.science/insu-03217099

Submitted on 4 May 2021

HAL is a multi-disciplinary open access archive for the deposit and dissemination of scientific research documents, whether they are published or not. The documents may come from teaching and research institutions in France or abroad, or from public or private research centers.

L'archive ouverte pluridisciplinaire **HAL**, est destinée au dépôt et à la diffusion de documents scientifiques de niveau recherche, publiés ou non, émanant des établissements d'enseignement et de recherche français ou étrangers, des laboratoires publics ou privés.

Check for updates

AGU100 ADVANCING EARTH AND SPACE SCIENCE

JGR

Journal of Geophysical Research: Space Physics

RESEARCH ARTICLE
10.1029/2018JA025879

Selective Attenuation of Lightning-Generated Whistlers at Extralow Frequencies: DEMETER Spacecraft Observations

J. Záhlava[1], F. Němec[1], O. Santolík[1,2], I. Kolmašová[1,2], M. Parrot[3], and D. Kouba[2]

[1]Faculty of Mathematics and Physics, Charles University, Prague, Czech Republic, [2]Department of Space Physics, Institute of Atmospheric Physics, The Czech Academy of Sciences, Prague, Czech Republic, [3]LPC2E/CNRS, Orléans, France

Key Points:
- We analyze ELF events formed by lightning-generated whistlers with intensity significantly reduced at specific frequencies
- We perform a study of 263 events identified in the DEMETER spacecraft data, including their detailed wave analysis
- We suggest that the events might be created in the waveguide formed around the refractive index maximum in the lower ionosphere

Correspondence to:
J. Záhlava,
jan.zahlava@gmail.com

Citation:
Záhlava, J., Němec, F., Santolík, O., Kolmašová, I., Parrot, M., & Kouba, D. (2018). Selective attenuation of lightning-generated whistlers at extralow frequencies: DEMETER spacecraft observations. *Journal of Geophysical Research: Space Physics*, *123*, 8631–8640. https://doi.org/10.1029/2018JA025879

Received 10 JUL 2018
Accepted 5 SEP 2018
Accepted article online 6 SEP 2018
Published online 8 OCT 2018

©2018. American Geophysical Union. All Rights Reserved.

Abstract Frequency-time spectrograms measured by the Detection of Electro-Magnetic Emissions Transmitted from Earthquake Regions (DEMETER) spacecraft (2004–2010, altitude about 700 km) at frequencies below 20 kHz sometimes contain lightning-generated whistlers whose intensity is significantly reduced at specific frequencies. The frequencies of the reduced intensity vary smoothly over the event duration, forming apparent curves in frequency-time spectrograms. Events at frequencies higher than the Earth-ionosphere waveguide cutoff frequency were explained by the interference of the first few waveguide modes of lightning-generated spherics propagating therein (Záhlava et al., 2015, https://doi.org/10.1002/2015JA021607. Here we present an analysis of events observed at frequencies lower than about 1 kHz. Altogether, we analyze 263 events identified at the times when DEMETER operated in the burst mode. The vast majority of the events (95%) took place during the nighttime, and they occurred more frequently during spring/autumn than during winter/summer. We present an overview of event properties. Moreover, measurements of all six electromagnetic field components performed by DEMETER allow us to perform a detailed wave analysis. It is shown that the emissions propagate with high wave normal angles inclined toward the Earth. We suggest that the events might be due to the wave propagation in the ionospheric waveguide formed around the refractive index maximum at the altitude of about 105 km.

1. Introduction

Over its more than 6-year-long (2004–2010) lifetime, the low-altitude DEMETER (Detection of Electro-Magnetic Emissions Transmitted from Earthquake Regions) spacecraft recorded many interesting electromagnetic wave phenomena. Focusing primarily on the very low frequency (VLF) range (up to 20 kHz), Parrot et al. (2015) compiled a set of most curious and at that time not understood particularities discovered in the frequency-time spectrograms of power spectral density of electric/magnetic field fluctuations. For the present study, the events similar to that shown in their Figure 12 are of a particular interest. Those events consist of many nearly horizontal curves of a reduced power spectral density of electric field fluctuations. Their detailed properties and possible formation mechanism were described by Záhlava et al. (2015). An example of such event measured on 22 September 2007 between 22:56:07 and 23:29:28 UT is shown in Figure 1. The red rectangle in the color-coded frequency-time spectrogram of power spectral density of electric field fluctuations marks the frequency-time interval of the event. In a more detailed spectrogram, one can recognize that the event is formed by lightning-generated spherics attenuated at specific, smoothly varying frequencies. Rather similar events were reported by Parrot et al. (2008) and El-Lemdani Mazouz et al. (2011). These events, with a striking V-shaped signature, were usually observed in the very proximity of intense thunderstorms. Although their distances from the thunderstorms are different, the mechanisms of their formation seem to be similar, related to the attenuation of lightning-generated emissions during their propagation in the Earth-ionosphere waveguide. Parrot et al. (2008) used a full-wave calculation of this propagation in order to model the V-shaped events in detail. Basic properties of the events can be, however, reproduced using a simplified waveguide mode theory (e.g., Budden, 1961) as shown by Záhlava et al. (2015). They evaluate the power spectral density of the sum of first two modes of the Earth-ionosphere waveguide as a function of distance between the spacecraft and the source storm obtaining a spectrogram qualitatively similar to the events analyzed.

In the present study, we analyze another type of events formed by attenuated lightning-generated spherics. Although the frequency-time structure of the events is rather similar to the events analyzed before, they

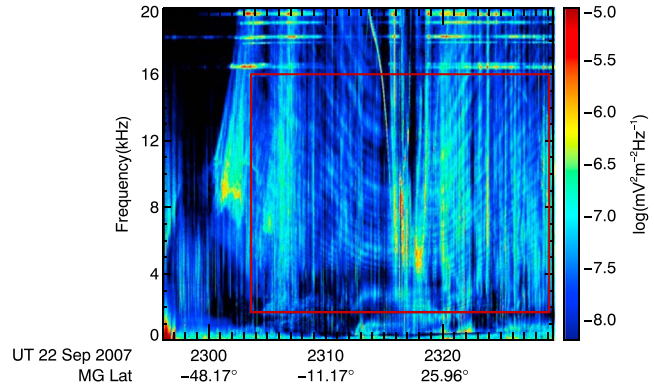


Figure 1. Frequency-time spectrogram of power spectral density of electric field fluctuations measured by the Detection of Electro-Magnetic Emissions Transmitted from Earthquake Regions spacecraft on 22 September 2007 between 22:56:07 and 23:29:28 UT. The red rectangle shows a frequency-time interval containing an example of the very low frequency events studied by Záhlava et al. (2015).

are observed at much lower frequencies, well in the extremely low frequency (ELF) range of the DEMETER spacecraft (up to 1.25 kHz). An example of such ELF event observed on 12 April 2010 between 19:32:35 UT and 19:36:00 UT is shown in Figure 2. The frequency-time interval of the event is again marked by the red rectangle. The similar structure of many bands of alternating enhanced and reduced power spectral density suggests that the way of event formation might be possibly similar to the formerly analyzed VLF events. However, as the events are observed at frequencies well below the Earth-ionosphere waveguide cutoff frequency, the formation mechanism suggested for the VLF events clearly cannot be straightforwardly applied. The ELF events might, nevertheless, result from a propagating of spherics in a different waveguide.

Smith et al. (1966) described a structure in the Earth's ionosphere capable of guiding electromagnetic waves at frequencies of about 5.25 kHz. They showed that waves at frequencies between the local minimum of the lower hybrid resonant (LHR) frequency and the closest LHR maximum propagating at large wave normal angles can be effectively trapped. The altitude region where the trapping takes place is therein called *Region II*, and it is characterized by a large refractive index of the trapped electromagnetic waves. This concept is further discussed by Gross (1970). The possible guiding of waves in the range of ultralow/extremely low frequencies was theoretically studied by, for example, Tepley and Landshoff (1966), Greifinger and Greifinger (1968), and Waters et al. (2013). These works focus on a waveguide formed around the minimum of Alfvén speed at the altitudes of about 300–400 km, known as ionospheric Alfvén resonator. The analysis made by Simões et al. (2012) supports the theoretical predictions and modeling. However, only frequencies up to several hertz are usually discussed. Recently, Chen et al. (2017) presented a ray-tracing analysis regarding our frequency range of interest, demonstrating that ELF waves can be also guided in the ionosphere.

2. Data Sets

The French microsatellite DEMETER operated between July 2004 and December 2010. The altitude of its polar orbit was changed from the original 710 to 660 km in December 2005. Due to the specific orbit trajectory, the measurements were performed in two distinct local time intervals, one around 10:30 LT and the other around 22:30 LT. DEMETER was capable of measuring both electric (Berthelier et al., 2006) and magnetic (Parrot et al., 2006) field fluctuations. Given the limited telemetry, the spacecraft alternated between two operation modes. In its Survey mode, DEMETER recorded data nearly continuously at invariant latitudes between −65° and 65°. Frequency-time spectrograms of power spectral density of fluctuations of one electric field component and one magnetic field component are available in this mode with the time resolution of 2.048 s, and the frequency resolution of about 19.53 Hz in the frequency range up to 20 kHz. While flying over selected areas of interest, the burst mode was active and waveforms of one electric field component and one magnetic field component were recorded with the sampling rate of 40 kHz. Additionally, in the burst mode, waveforms of all six electromagnetic field components are available with a sampling rate of 2.5 kHz. Such multicomponent measurements allow for a calculation of detailed wave propagation parameters (Santolík & Parrot, 1998, 1999; Santolík et al., 2003, 2006).

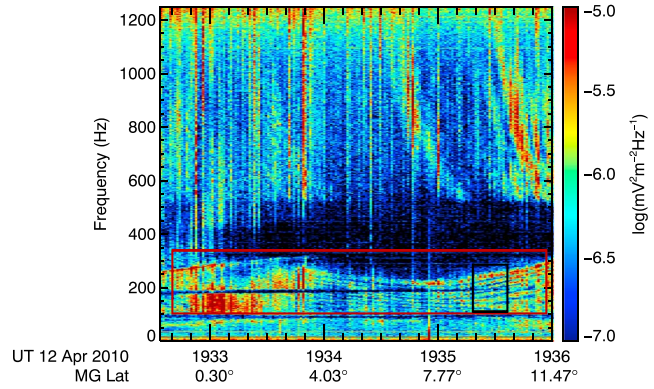


Figure 2. Frequency-time spectrogram of power spectral density of electric field fluctuations measured by the Detection of Electro-Magnetic Emissions Transmitted from Earthquake Regions spacecraft on 12 April 2010 from 19:32:35 UT to 19:36:00 UT. The red rectangle marks a frequency-time interval of an example of the studied extremely low frequency events. Moreover, part of the event selected for a detailed analysis as well pronounced and unbiased by other wave phenomena is framed by the black rectangle.

Additionally, lightning occurrence rate data obtained by the Optical Transient Detector/Lightning Imaging Sensor (OTD/LIS) mission (Cecil et al., 2014) are used in the present paper. The used data set provides us with the average lightning occurrence maps with the spatial resolution of 2.5° in both the geographic latitude and longitude and the local time resolution of 2 hr for each day of the year. These daily geographic maps were recalculated to geomagnetic coordinates, preserving the same spatial and temporal resolution.

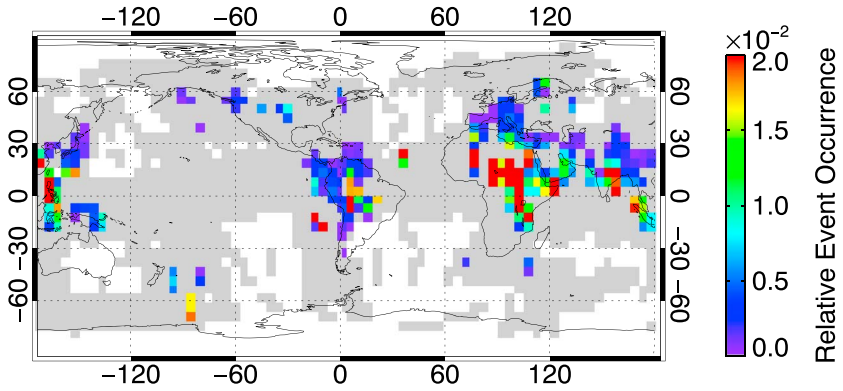


Figure 3. Color-coded geomagnetic map of a relative occurrence of the events. Each 5° × 5° bin shows the ratio of the total event duration to the total time of burst mode measurements. The white color represents the areas with no burst mode measurements. The gray color represents the areas with no events.

Coming back to the example event from Figure 2, a set of U-shaped curves of alternating enhanced and reduced power spectral density is observed at frequencies between about 100 and 300 Hz. The frequency spacing between these curves apparently decreases close to the time corresponding to the bottom of the U shape. Accordingly, the bandwidth of individual curves can be seen to increase on the sides, observable in particular on the right-hand side. The individual curves forming the event can be particularly well distinguished in the frequency-time subinterval marked by the black rectangle. This interval, where the event is unspoiled by other wave phenomena, was selected for a further detailed wave analysis (see later in Figure 7).

All of the available 56,788 ELF burst-time spectrograms, most of which last from 1 to 7 min, were visually inspected for the presence of the U-shaped spheric attenuation events. In total, about 3,416 hr of measurements were processed. Overall, 263 such events were identified. Most of them (249) occurred during the nighttime half orbits. Additionally, 244 frequency-time subintervals were classified as unspoiled by other wave phenomena and selected for a detailed analysis. For each identified event and for each selected unspoiled frequency-time subinterval, minimal and maximal frequencies and beginning and ending times were determined. These are used as a starting point of the presented analysis. We note that only four of the ELF events took place at the same time as the VLF events analyzed by Záhlava et al. (2015).

3. Results

A geomagnetic map of event occurrence is shown in Figure 3. Color coded according to the scale on the right-hand side is the total duration of events normalized by the overall duration of DEMETER burst mode data in each 5° × 5° bin. White areas in the map show places where no burst mode measurements were

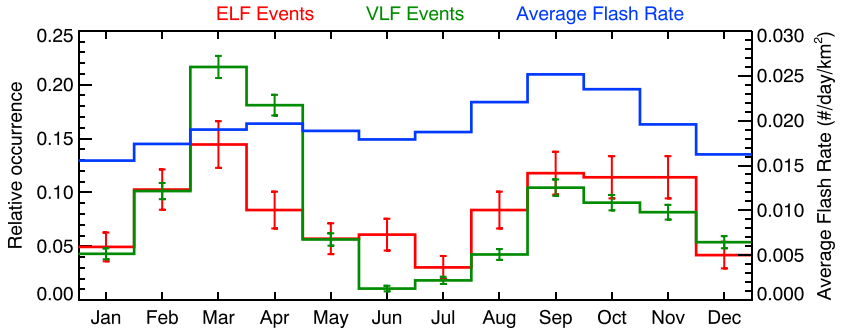


Figure 4. Seasonal variation of the occurrence of ELF (red) and previously studied VLF (green) events (Záhlava et al., 2015). The numbers of events in individual months are normalized by the total number of events. The error bars show one standard deviation. The blue line shows the average flash rate at geomagnetic latitudes lower than 30° and at geomagnetic longitudes from −20° to 20° and from 70° to 220°, where the events are predominantly observed. ELF = extremely low frequency; VLF = very low frequency.

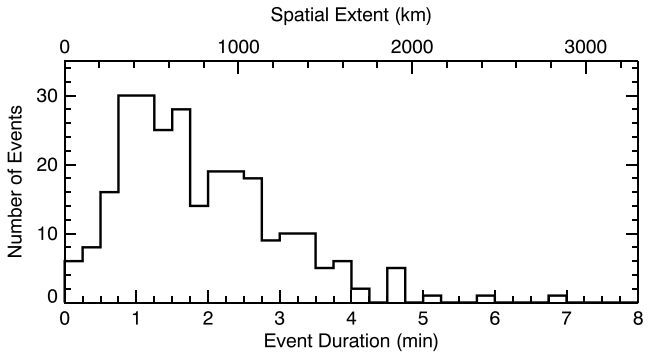


Figure 5. Histogram of the observed event durations. The spatial scale at the top was calculated from the observed event durations using the spacecraft orbital velocity.

performed. The gray color represents the regions where no events were detected, although the burst mode measurements were performed. It can be seen that most of the events take place at low geomagnetic latitudes, and they occur primarily over the landmass. One can identify three main areas where the events occur: (i) equatorial part of South America, (ii) central Africa and Europe, which is smoothly joined with (iii) equatorial Asia.

Figure 4 compares seasonal dependences of the analyzed ELF events (red) with VLF events studied by Záhlava et al. (2015; green). The fractions of the total number of events which took place in individual months are displayed; that is, the sum of values in individual columns is by definition equal to 1. The error bars displayed correspond to a standard deviation derived from a Poisson distribution as $\sigma = \sqrt{p(1-p)/N}$, where N is the total number of events and p is the relative occurrence of events in a given month. The similarity between the two seasonal dependences is striking with the occurrence rate peaks in the northern spring and autumn. For a comparison, the average OTD/LIS flash rate in the areas where the events mainly occur is plotted by the blue line using the scale on the right-hand ordinate. Specifically, only the flash rates within 30° from the geomagnetic equator and in two intervals of geomagnetic longitude, from −20° to 20° and between 70° and 220°, were considered. Additionally, given that the vast majority of the events takes place on the nightside, only the OTD/LIS data between 20:00 LT and 24:00 LT were used. Similar to the occurrence of events, also the flash rate peaks in the Northern Hemisphere autumn. However, the northern spring flash rate peak is extremely weak, nearly nonexistent.

A histogram of event durations is shown in Figure 5. The events are usually detected for several minutes. Given the DEMETER circular orbit, the upper abscissa shows the corresponding spatial extent. While observing the events, DEMETER usually covered distances from about 200 up to about 1,500 km. One should also note that—at least in some events—the observed event duration is limited by the burst mode coverage. While the minimal frequency of VLF event analyzed by Záhlava et al. (2015) was related to the cutoff frequency of the Earth-ionosphere waveguide, the minimal frequencies of the ELF events are typically below 500 Hz, as shown by the green histogram in Figure 6a. As for the maximal frequencies of the ELF events shown by the red line in Figure 6a, there is a group of events limited to frequencies below only about 100 to 500 Hz. The other large group of events extends up to the highest analyzed frequency (1.25 kHz). An inspection of relevant VLF burst mode data reveals that nine of these events actually extend above 1.25 kHz, reaching about 1.5 kHz. A single

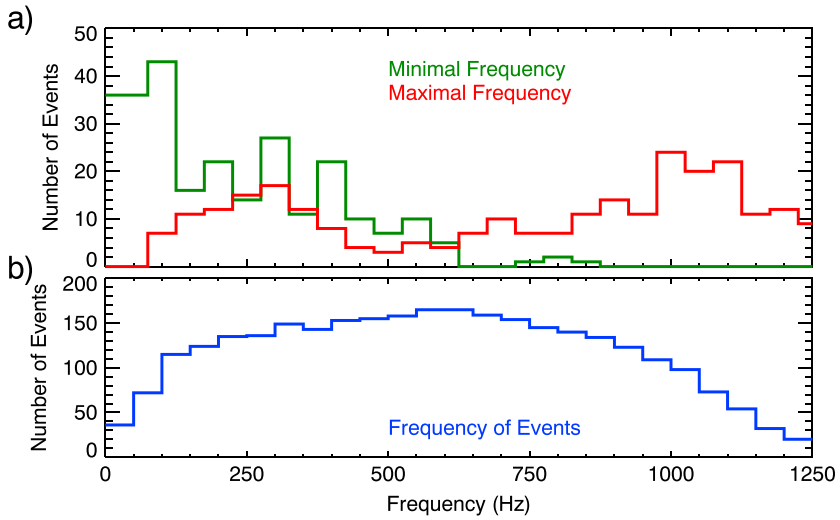


Figure 6. (a) Histogram of minimal (green) and maximal (red) frequencies of the events. (b) Cumulative histogram of event frequencies; that is, the total number of events which spanned over a given frequency is shown.

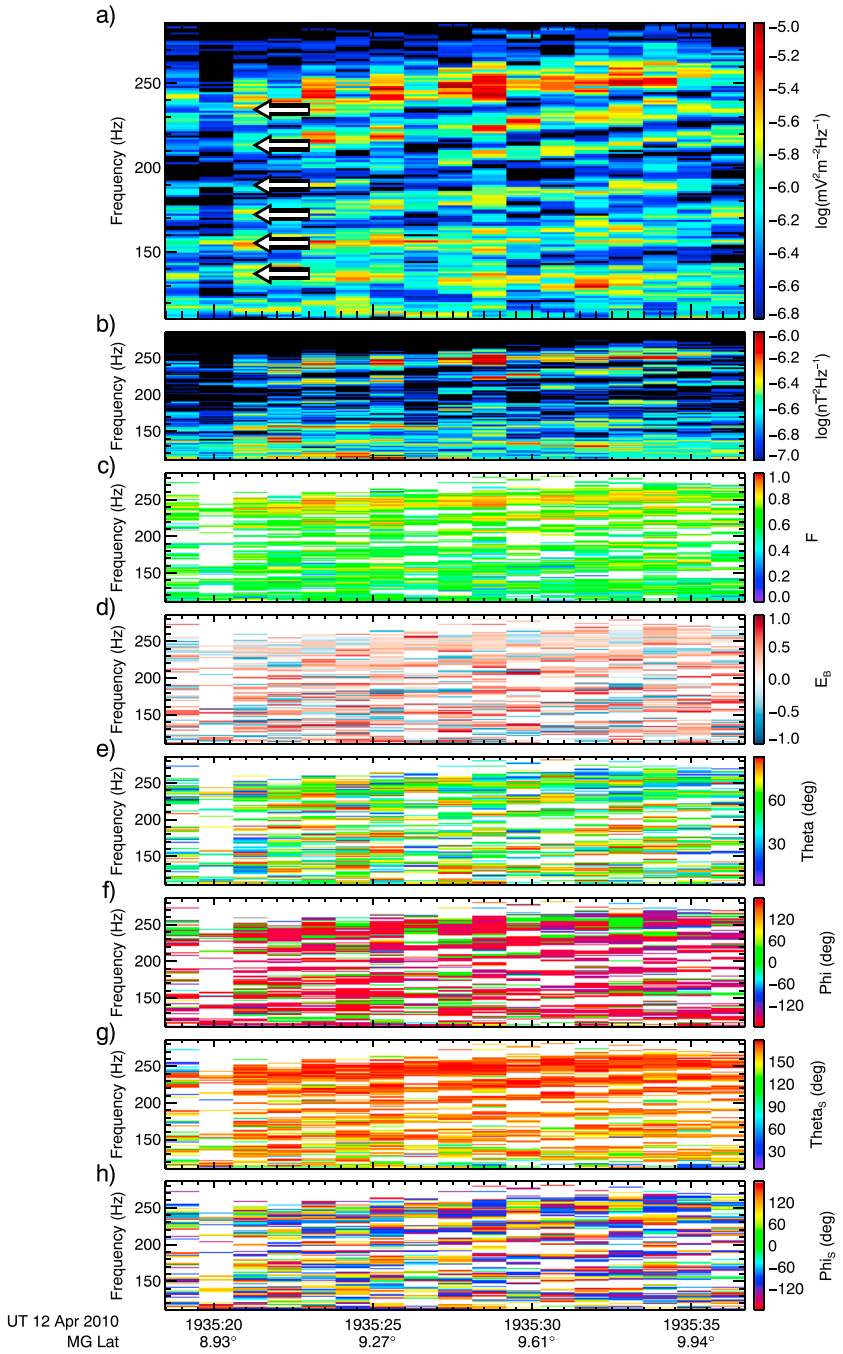


Figure 7. (a) Frequency-time spectrogram of power spectral density of electric field fluctuations. Frequencies of individual spectral maxima are marked by the white arrows. (b) Frequency-time spectrogram of power spectral density of magnetic field fluctuations. (c) Planarity of magnetic field fluctuations. (d) Ellipticity of magnetic field fluctuations. (e) Wave normal angle with respect to the ambient magnetic field. (f) Azimuth of the wave normal. (g) Angle between the Poynting vector and the ambient magnetic field. (h) The azimuthal direction of the Poynting vector. The measurements were taken on 12 April 2007 between 19:35:18 and 19:35:37 UT, corresponding to the frequency-time subinterval from Figure 2 marked by the black rectangle.

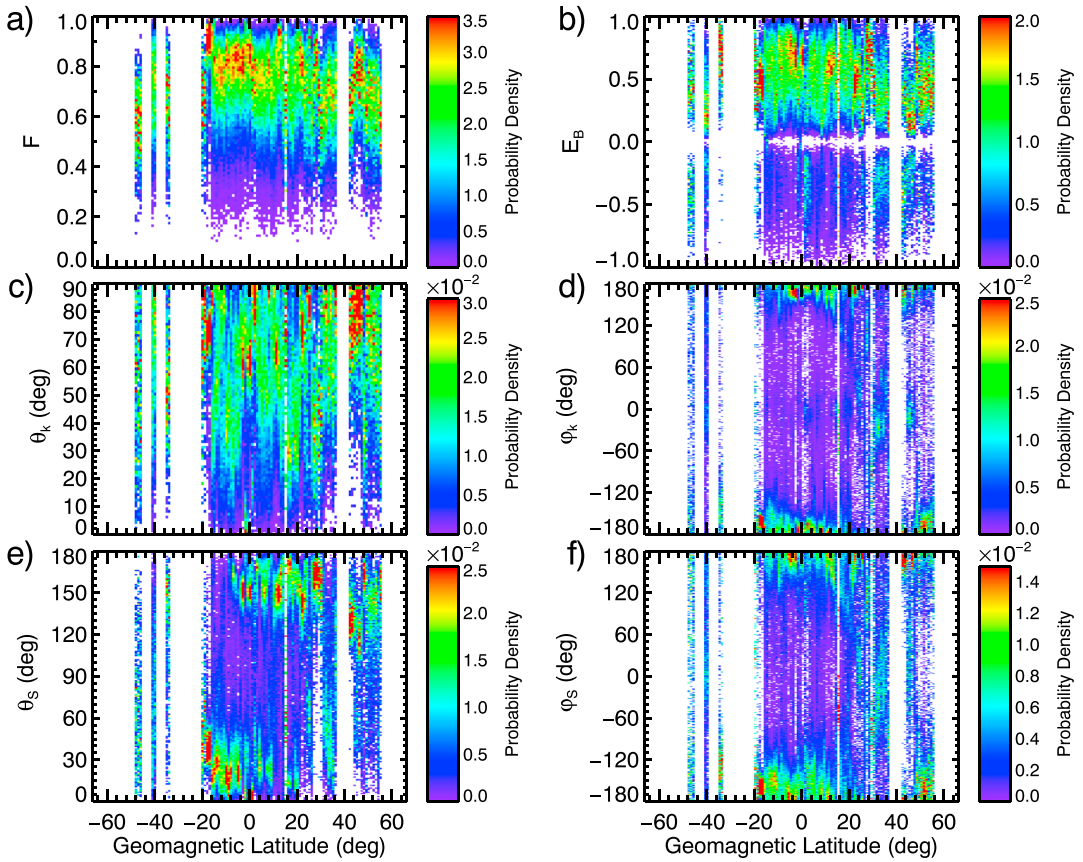


Figure 8. Color-coded probability density of (a) planarity of magnetic field fluctuations, (b) ellipticity of magnetic field fluctuations, (c) wave normal angle with respect to the ambient magnetic field, (d) azimuth of the wave normal, (e) angle between the Poynting vector and the ambient magnetic field, and (f) the azimuthal direction of the Poynting vector as a function of geomagnetic latitude.

event was found to extend up to 2 kHz. A histogram of frequencies where the events were observed shown in Figure 6b demonstrates that they span nearly uniformly over all frequencies up to about 1 kHz.

Results of a detailed wave analysis performed for the example event from Figure 2 are shown in Figure 7. Figures 7a and 7b show color-coded power spectral density of electric and magnetic field fluctuations, respectively. Figure 7c shows the planarity of magnetic field fluctuations, that is, the ratio of the shortest and the longest axes of the polarization ellipsoid (Santolík et al., 2003). The values equal to 1 would correspond to an ideal plane wave. The ellipticity of magnetic field fluctuations is shown in Figure 7d (Santolik & Gurnett, 2002). Positive values of ellipticity correspond to right-handed polarized waves, whereasnegative values correspond to left-handed polarization. The absolute values of 1 and 0 correspond to circular and linear polarization, respectively. Figure 7e depicts the color-coded wave normal angles with respect to the ambient magnetic field (Santolík et al., 2003), and Figure 7f the azimuth of the wave normal. Finally, Figure 7g shows the angle between the Poynting vector and the ambient magnetic field, and Figure 7h shows its azimuthal direction (Santolík et al., 2010). The azimuth angle of ±180° corresponds to the Earthward propagation. Additionally, the white arrows in Figure 7a mark the frequencies of the six intensity maxima visually identified in the spectrum. Note that only frequency-time intervals with power spectral density of electric field fluctuations larger

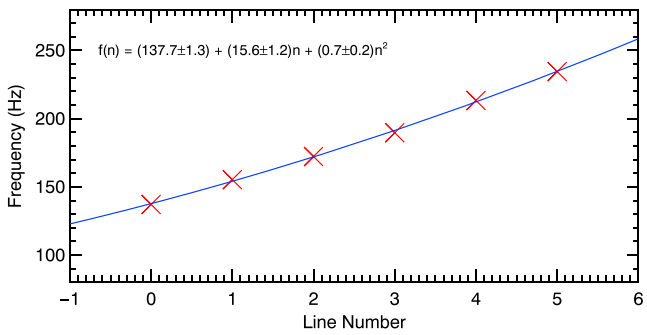


Figure 9. Frequencies of the spectral maxima marked by white arrows in Figure 3a as a function of their order are shown by the red crosses. The blue line corresponds to the best quadratic fit.

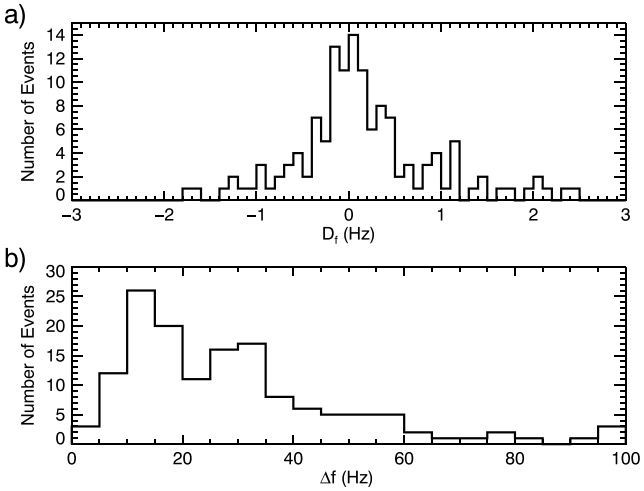


Figure 10. (a) Histogram of the fit parameters D_f. (b) Histogram of the fit parameter Δf.

than an intensity threshold were included in the analysis in Figure 7. This intensity threshold was set manually to 4×10^{-7} $mV^2 \cdot m^{-2} \cdot Hz^{-1}$ for this event in order to eliminate all but the intense frequency-time intervals. Further, only frequency-time intervals with the planarity of magnetic field fluctuations larger than 0.5 were analyzed in order to ensure the validity of the planar wave approximation used for the calculation of wave propagation parameters. This planarity threshold is not applied in Figure 7c, which allows us to investigate the influence of this additional restriction on the number of data points. One can see that there is only a marginal amount of blueish frequency-time intervals with large enough intensity but not large enough planarity. As for the wave polarization, red color prevails in Figure 7d, which means that the event is formed primarily by right-handed polarized waves. Figure 7e shows that the waves forming the event propagate with rather oblique wave normal angles with respect to the ambient magnetic field. Finally, Figures 7g and 7h demonstrate that they propagate obliquely toward the geomagnetic equator with a rather ambiguous azimuthal direction.

After performing this detailed wave analysis for each of the 244 selected frequency-time intervals, we evaluated probability densities of the values of the six discussed propagation parameters. These are shown in Figure 8 as a function of geomagnetic latitude. The intensity thresholds were again manually set for each of these events. Similarly as in Figure 7c, Figure 8a contains also the planarity values lower than 0.5, which, however, occur rarely. Figure 8b shows a distribution of the ellipticity of magnetic field fluctuations. The right-handed polarization is dominant at all geomagnetic latitudes. Figure 8c shows that the waves forming the events propagate with highly oblique wave normal angles, and Figure 8d shows that the wave vector is usually inclined toward the Earth. None of the four analyzed wave parameters exhibits a significant dependence on the geomagnetic latitude. However, the angle between the Poynting vector and the ambient magnetic field depicted in Figure 8e exhibits a striking change of its behavior just at the magnetic equator. While the waves forming the events in the Southern Hemisphere propagate nearly along the ambient magnetic field, the events in the Northern Hemisphere propagate opposite to the ambient magnetic field. The waves forming the events thus in both cases propagate toward the magnetic equator. Moreover, Figure 8f shows that the Poynting vector is inclined toward the lower L shells in most cases. The statistical results depicted in Figure 8 therefore demonstrate that the case shown in Figure 7 is rather typical.

We further investigated frequency characteristics of the events. For each of the selected frequency-time intervals unspoiled by other wave phenomena, we visually identified its individual spectral maxima, and we plotted their frequencies as a function of their order n, lowest to highest frequency starting at $n = 0$. As the frequency spacing between consecutive intensity maxima is generally not strictly constant but sometimes exhibits a systematic bend, we fitted the dependence by a quadratic form:

$$f(n) = f_0 + \Delta_f \cdot n + D_f \cdot n^2, \quad (1)$$

where f_0 is the frequency of zero-order spectral maximum, Δ_f is the frequency spacing between the first two maxima, and D_f is proportional to the frequency spacing change toward higher-order n. The result of this analysis for the example interval from Figure 7 are shown in Figure 9. It can be seen that in this particular case, the frequency separation of consecutive spectral maxima slightly increases with the order n. Histograms of the obtained values of D_f and Δ_f are shown in Figures 10a and 10b, respectively. Figure 10a demonstrates that both frequency spacing increases and decreases are possible, and they occur in approximately the same number of events. We note that the determination of the frequencies of the spectral maxima is often rather inaccurate, with an uncertainty comparable to observed frequency spacing variations. Figure 10b shows that the frequency spacings between consecutive spectral maxima usually range from about 5 Hz up to about 60 Hz.

4. Discussion

The analyzed ELF events consist of several alternating frequency bands of enhanced and reduced power spectral density of electric field fluctuations of detected lightning-generated spherics. As shown in Figure 10b, the frequency spacing between consecutive spectral maxima significantly varies. The broadness of the frequency

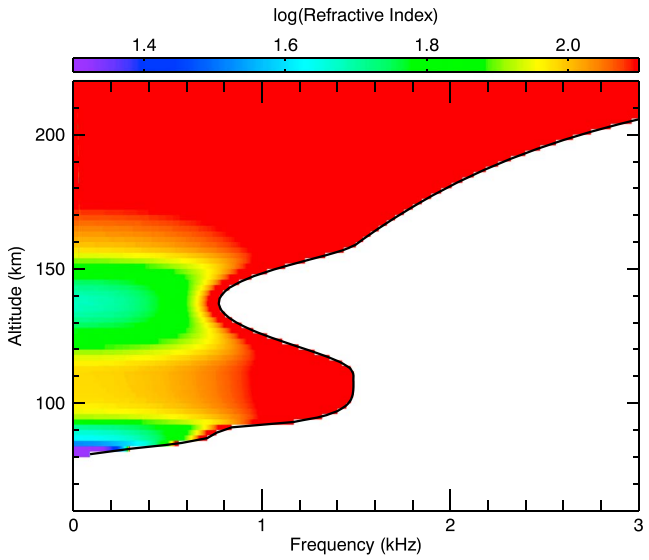


Figure 11. Color coded refractive index of a perpendicularly propagating wave as a function of frequency (abscissa) and altitude (ordinate).

spacing distribution has two main possible explanations: (i) Frequency spacing between the spectral maxima depends on the exact frequency-time subinterval in which the detailed wave analysis was possible. Namely, the further we are from the bottom of the U shape, the further apart in frequency are the consecutive spectral maxima. Additionally, given the possible overlaying by another wave phenomenon, only higher-order spectral maxima might be visible which might also, in certain cases, influence the base frequency spacing. (ii) The structures taking part in the event formation might be rather unstable, and the variation of their properties might be therefore substantial for the event parameters. The shape of the ELF events in frequency-time spectrograms is quite similar to the previously studied VLF events formed by a wave mode interference of lightning-generated spherics in the Earth-ionosphere waveguide (Záhlava et al., 2015). The seasonal dependence of the two types of events is also similar with the maximum event occurrence during the northern spring and autumn. This might suggest that the generation mechanisms of the two types of events might be similar. On the other hand, the frequency range and observed event durations significantly differ. Given that the frequency of the ELF events is well below the critical frequency of the Earth-ionosphere waveguide, and assuming an analogical event formation based on the mode interference, one needs to look for a waveguide with properties appropriate for the characteristics of the ELF events. Specifically, the cutoff frequency of this hypothetical waveguide should be in the order of tens to hundreds of hertz. Moreover, given the variance of the event characteristics, one might expect that the properties of the waveguide are not very stable.

We suggest that such a waveguide might be formed in the ionosphere at altitudes around the local maximum of the refractive index of the R-X whistler-mode waves (Stix, 1992) propagating nearly perpendicularly to the ambient magnetic field. In order to demonstrate that such refractive index condition indeed exists in the ionosphere, we use the International Reference Ionosphere model (Bilitza et al., 2014) to calculate frequency dependence of the refractive indices of perpendicularly propagating waves over a wide range of altitudes. Although the exact model output depends slightly on the date and location, all the nighttime results are qualitatively very similar. A representative example of the obtained refractive index dependences, which corresponds to the example event, is depicted in Figure 11. The ionospheric profile was obtained over central Africa during the nighttime half orbit of DEMETER. It shows a color-coded refractive index of waves with wave normals perpendicular to the ambient magnetic field as a function of altitude (ordinate) and frequency (abscissa). The resolution of the plot is 2 km in altitude and 50 Hz in frequency. The black curve represents the LHR frequency. The refractive index maximum at frequencies below about 1 kHz at altitudes of about 105 km is of the main interest for our analysis.

Considering a wave propagating nearly horizontally, it becomes trapped in this altitudinal region with large refractive index, being specularly reflected at altitudes both below and above. Such a propagation then resembles the normal waveguide propagation, and the appropriate waveguide critical frequency can be estimated. Considering a wave with a representative frequency of 0.5 kHz, we calculate the corresponding optical path s as

$$s = \int_{h=90\ \mathrm{km}}^{h=120\ \mathrm{km}} n(h)\mathrm{d}h, \tag{2}$$

where h is the altitude and $n(h)$ is the appropriate refractive index. The lower and upper bounds were estimated based on the refractive index altitudinal profile as altitudes where the refractive index sharply decreases. The obtained values were typically on the order of about 3,000 km, which, when considered as a dimension of the waveguide, results in a critical frequency of $f_c = c/(2s) \approx 50$ Hz (see, e.g., Budden, 1961). Such a critical frequency would be then in a rough agreement with the observed properties of the ELF events. Specifically, the event frequencies would be larger than twice the waveguide critical frequency (Záhlava et al., 2015), and their frequency spacing compared to the VLF events should be appropriately lower. We thus suggest that the lightning-generated spherics become trapped in this ionospheric waveguide at altitudes of about 100–110 km, where the refractive index has a local maximum, propagating nearly horizontally and

almost perpendicular to the ambient magnetic field. The feeding of this ionospheric waveguide might possibly require a wave scattering on density inhomogeneities in order to change the wave directions in such a way that they become trapped. The propagation in this ionospheric waveguide then, due to the modal interference, results in a selective attenuation of certain wave frequencies at a given distance. After escaping from the waveguide and being detected by the spacecraft, a characteristic event spectrum is thus observed. The event shape in the frequency-time spectrograms then corresponds, following Záhlava et al. (2015), to the distance which the waves propagated in the ionospheric waveguide before being detected by DEMETER. Note that the spacecraft is at an altitude of about 600 km above the waveguide, and the observed wave propagation properties thus do not correspond to the waveguide trapping and do not allow us to confirm the suggested event formation more thoroughly. It is, nevertheless, rather suspicious that the observed wave properties suggest the emissions to come from larger geomagnetic latitudes and, possibly, also from larger radial distances. This seems to contradict a direct wave propagation from the low altitudes of the waveguide to DEMETER. A detailed theoretical investigation of the waveguide formation, its feeding, and the propagation of electromagnetic waves eventually escaping from it is clearly needed. This is, however, beyond the scope of this experimental paper presenting the first analysis of this wave phenomenon.

Finally, we tried to identify most favorable conditions for the events to occur. However, none of the investigated properties seems to change significantly at the times of the events. Namely, we studied a possible dependence of the event occurrence on the geomagnetic activity, lightning activity, and whistler occurrence rate. For each event, evolutions of both *AE* and *Kp* indices were analyzed over a time interval from 1 day before to 1 day after the event. However, no clear systematic variation of the geomagnetic activity around the times of the events was found. Superposed epoch analysis, that is, the time variation of the average *AE*/*Kp* index as a function of the time relative to the events also did not exhibit any significant variation. To investigate a possible correlation between the events and lightning occurrence, World Wide Lightning Location network data, which provide us with the times and locations of individual lightning strokes occurring worldwide (Rodger et al., 2006), were used. We compared the positions of individual lightning strokes which occurred during the event duration with the spacecraft footprint. The same was done also for several days before/after the event, using the same spacecraft location and time of the day. Assuming that the event occurrence is related to a higher lightning activity, one would expect to see the lightning occurrence to be larger during the events than several days before/after. However, no such enhancement could be identified. Finally, we compared the event occurrence with the whistler data provided by the neural network for whistler detection on board DEMETER (Elie et al., 1999). Additionally, given the Sun synchronization of its polar orbit, it covers nearly the same location every day at about the same local time. We thus evaluate the whistler occurrence rate measured roughly at the event location 1 day before and 1 day after the event, and we compare it with the whistler occurrence rate during the event. However, no significant change of the whistler occurrence rates during the events was identified. Another possible way how to feed the ionospheric waveguide might be electromagnetic emissions coming from larger radial distances. Equatorial noise emissions were shown to occasionally propagate down to the altitudes of DEMETER (Santolík et al., 2016). This, however, occurs predominantly during enhanced geomagnetic activity (Němec et al., 2016), and, moreover, such emissions would be expected to propagate away from the equator. Another possible source might be low-altitude hiss propagating toward the geomagnetic equator (Chen et al., 2017).

We further analyzed a potential association of the studied events with ionospheric disturbances. The data from the Digital Ionogram DataBase GIRO (Global Ionospheric Radio Observatory) (Reinisch & Galkin, 2011) was used. Altogether, 22 events with ionosondes in reasonable distance were identified based on the station and event locations and the data availability in the GIRO database. We investigated whether the ionospheric profiles at the times of the events differ from those obtained shortly before/after the times of the events and 1 day before/after the times of the events. However, no systematic relation between the ionospheric profiles and the event occurrence was identified.

5. Summary

All available burst-mode spectrograms obtained by the DEMETER spacecraft in the ELF range were visually inspected, and overall 263 events with a reduced intensity of lightning-generated spherics were identified. Additionally, 244 frequency-time subintervals where the events were unspoiled by other natural emissions were identified and subjected to a detailed wave analysis. It appears that the observed events occur preferably over the landmass, and they are concentrated in the proximity of the geomagnetic equator. As for the sea-

sonal dependence, they follow the distribution of previously studied VLF events, i.e., more events occur in the northern spring and autumn. Detailed analysis of wave propagation properties and spectral maxima of the selected frequency-time subintervals shows that the events are formed by right-hand polarized waves propagating with high wave normal angles inclined toward the Earth's surface. The frequency spacing between consecutive spectral maxima may be very different from event to event. In some cases it is not constant, but it rather changes as a function of frequency. We suggested that the events might be formed due to the modal interference in the waveguide formed at altitudes around the refractive index maximum in the lower ionosphere.

Acknowledgments
DEMETER was a CNES mission. We thank the engineers from CNES and scientific laboratories (CBK, IRAP, LPC2E, LPP, and SSD of ESTEC) who largely contributed to the success of this mission. DEMETER data are accessible at https://sipad-cdpp.cnes.fr. We thank B. W. Reinisch for administration of the GIRO database. The data are accessible at http://ulcar.uml.edu/DIDBase/. F. N. and J. Z. acknowledge the support of GACR grant 18-00844S and GAUK grant 300216. The work of O. S. and I. K. was supported by GACR grant 17-07027S and by the Praemium Academiae award from the CAS.

References

Berthelier, J.-J., Godefroy, M., Leblanc, F., Malingre, M., Menvielle, M., Lagoutte, D., et al. (2006). ICE, the electric field experiment on DEMETER. *Planetary and Space Science*, *54*(5), 456–471. https://doi.org/10.1016/j.pss.2005.10.016

Bilitza, D., Altadill, D., Zhang, Y., Mertens, C., Truhlik, V., Richards, P., et al. (2014). The International Reference Ionosphere 2012—A model of international collaboration. *Journal of Space Weather and Space Climate*, *4*, A07. https://doi.org/10.1051/swsc/2014004

Budden, K. G. (1961). *The Wave-Guide Mode Theory of Wave Propagation*. MI: Logos Press.

Cecil, D. J., Buechler, D. E., & Blakeslee, R. J. (2014). Gridded lightning climatology from TRMM-LIS and OTD: Dataset description. *Atmospheric Research*, *135*, 404–414. https://doi.org/10.1016/j.atmosres.2012.06.028

Chen, L., Santolík, O., Hajoš, M., Zheng, L., Zhima, Z., Heelis, R., et al. (2017). Source of the low-altitude hiss in the ionosphere. *Geophysical Research Letters*, *44*, 2060–2069. https://doi.org/10.1002/2016GL072181

El-Lemdani Mazouz, F., Pincon, J.-L., Parrot, M., De Feraudy, H., Lehtinen, N. G., & Lefeuvre, F. (2011). Asymmetric V-shaped streaks recorded on board DEMETER satellite above powerful thunderstorms. *Journal of Geophysical Research*, *116*, A11321. https://doi.org/10.1029/2011JA016794

Elie, F., Hayakawa, M., Parrot, M., Pinçon, J.-L., & Lefeuvre, F. (1999). Neural network system for the analysis of transient phenomena on board the DEMETER micro-satellite. *IEICE TRANSACTIONS on Fundamentals of Electronics, Communications and Computer Sciences*, *82*(8), 1575–1581.

Greifinger, C., & Greifinger, P. S. (1968). Theory of hydromagnetic propagation in the ionospheric waveguide. *Journal of Geophysical Research*, *73*(23), 7473–7490. https://doi.org/10.1029/JA073i023p07473

Gross, S. H. (1970). VLF duct associated with the lower-hybrid-resonance frequency in a multi-ion upper ionosphere. *Journal of Geophysical Research*, *75*(22), 4235–4247. https://doi.org/10.1029/JA075i022p04235

Němec, F., Parrot, M., & Santolík, O. (2016). Equatorial noise emissions observed by the DEMETER spacecraft during geomagnetic storms. *Journal of Geophysical Research: Space Physics*, *121*, 9744–9757. https://doi.org/10.1002/2016JA023145

Parrot, M., Benoist, D., Berthelier, J. J., Blecki, J., Chapuis, Y., Colin, F., et al. (2006). The magnetic field experiment IMSC and its data processing onboard DEMETER: Scientific objectives, description and first results. *Planetary and Space Science*, *54*(5), 441–455. https://doi.org/10.1016/j.pss.2005.10.015

Parrot, M., Berthelier, J.-J., Blecki, J., Brochot, J., Hobara, Y., Lagoutte, D., et al. (2015). Unexpected very low frequency (VLF) radio events recorded by the ionospheric satellite DEMETER. *Surveys in Geophysics*, *36*(3), 483–511. https://doi.org/10.1007/s10712-015-9315-5

Parrot, M., Inan, U. S., & Lehtinen, N. G. (2008). V-shaped VLF streaks recorded on DEMETER above powerful thunderstorms. *Journal of Geophysical Research*, *113*, A10310. https://doi.org/10.1029/2008JA013336

Reinisch, B. W., & Galkin, I. A. (2011). Global Ionospheric Radio Observatory (GIRO). *Earth, Planets and Space*, *63*(4), 377–381. https://doi.org/10.5047/eps.2011.03.001

Rodger, C. J., Werner, S., Brundell, J. B., Lay, E. H., Thomson, N. R., Holzworth, R. H., & Dowden, R. L. (2006). Detection efficiency of the VLF World-Wide Lightning Location Network (WWLLN): Initial case study. *Annales Geophysicae*, *24*(12), 3197–3214. https://doi.org/10.5194/angeo-24-3197-2006

Santolik, O., & Gurnett, D. A. (2002). Propagation of auroral hiss at high altitudes. *Geophysical Research Letters*, *29*(10), 1481. https://doi.org/10.1029/2001GL013666

Santolík, O., Němec, F., Parrot, M., Lagoutte, D., Madrias, L., & Berthelier, J. J. (2006). Analysis methods for multi-component wave measurements on board the DEMETER spacecraft. *Planetary and Space Science*, *54*(5), 512–527. https://doi.org/10.1016/j.pss.2005.10.020

Santolík, O., & Parrot, M. (1998). Propagation analysis of electromagnetic waves between the helium and proton gyrofrequencies in the low-altitude auroral zone. *Journal of Geophysical Research*, *103*(A9), 20,469–20,480. https://doi.org/10.1029/98JA01386

Santolík, O., & Parrot, M. (1999). Case studies on the wave propagation and polarization of ELF emissions observed by Freja around the local proton gyrofrequency. *Journal of Geophysical Research*, *104*(A2), 2459–2475. https://doi.org/10.1029/1998JA900045

Santolík, O., Parrot, M., & Lefeuvre, F. (2003). Singular value decomposition methods for wave propagation analysis. *Radio Science*, *38*(1), 1010. https://doi.org/10.1029/2000RS002523

Santolík, O., Parrot, M., & Němec, F. (2016). Propagation of equatorial noise to low altitudes: Decoupling from the magnetosonic mode. *Geophysical Research Letters*, *43*, 6694–6704. https://doi.org/10.1002/2016GL069582

Santolík, O., Pickett, J. S., Gurnett, D. A., Menietti, J. D., Tsurutani, B. T., & Verkhoglyadova, O. (2010). Survey of Poynting flux of whistler mode chorus in the outer zone. *Journal of Geophysical Research*, *115*, A00F13. https://doi.org/10.1029/2009JA014925

Simões, F., Klenzing, J., Ivanov, S., Pfaff, R., Freudenreich, H., Bilitza, D., et al. (2012). Detection of ionospheric Alfvén resonator signatures in the equatorial ionosphere. *Journal of Geophysical Research*, *117*, A11305. https://doi.org/10.1029/2012JA017709

Smith, R. L., Kimura, I., Vigneron, J., & Katsufrakis, J. (1966). Lower hybrid resonance noise and a new ionospheric duct. *Journal of Geophysical Research*, *71*(7), 1925–1927. https://doi.org/10.1029/JZ071i007p01925

Stix, T. H. (1992). *Waves in Plasmas*. Basingstoke, UK: Springer Science & Business Media.

Tepley, L., & Landshoff, R. K. (1966). Waveguide theory for ionospheric propagation of hydromagnetic emissions. *Journal of Geophysical Research*, *71*(5), 1499–1504. https://doi.org/10.1029/JZ071i005p01499

Waters, C. L., Lysak, R. L., & Sciffer, M. D. (2013). On the coupling of fast and shear Alfvén wave modes by the ionospheric Hall conductance. *Earth, Planets and Space*, *65*(5), 385–396. https://doi.org/10.5047/eps.2012.08.002

Záhlava, J., Němec, F., Santolík, O., Kolmašová, I., Parrot, M., & Rodger, C. J. (2015). Very low frequency radio events with a reduced intensity observed by the low-altitude DEMETER spacecraft. *Journal of Geophysical Research: Space Physics*, *120*, 9781–9794. https://doi.org/10.1002/2015JA021607